Nanoscale Advances

ROYAL SOCIETY OF CHEMISTRY

PAPER

View Article Online
View Journal | View Issue

Cite this: *Nanoscale Adv.*, 2021, **3**, 4145

Local inhomogeneities resolved by scanning probe techniques and their impact on local 2DEG formation in oxide heterostructures†

M.-A. Rose, *[ab] J. Barnett, [c] D. Wendland,[c] F. V. E. Hensling, [b] J. M. Boergers, [b] M. Moors, [b] R. Dittmann, [b] T. Taubner [c] and F. Gunkel *[ab]

Lateral inhomogeneities in the formation of two-dimensional electron gases (2DEG) directly influence their electronic properties. Understanding their origin is an important factor for fundamental interpretations, as well as high quality devices. Here, we studied the local formation of the buried 2DEG at $LaAlO_3/SrTiO_3$ (LAO/STO) interfaces grown on STO (100) single crystals with partial TiO_2 termination, utilizing *in situ* conductive atomic force microscopy (c-AFM) and scattering-type scanning near-field optical microscopy (s-SNOM). Using substrates with different degrees of chemical surface termination, we can link the resulting interface chemistry to an inhomogeneous 2DEG formation. In conductivity maps recorded by c-AFM, a significant lack of conductivity is observed at topographic features, indicative of a local SrO/AlO_2 interface stacking order, while significant local conductivity can be probed in regions showing TiO_2/LaO interface stacking order. These results could be corroborated by s-SNOM, showing a similar contrast distribution in the optical signal which can be linked to the local electronic properties of the material. The results are further complemented by low-temperature conductivity measurements, which show an increasing residual resistance at 5 K with increasing portion of insulating SrO-terminated areas. Therefore, we can correlate the macroscopic electrical behavior of our samples to their nanoscopic structure. Using proper parameters, 2DEG mapping can be carried out without any visible alteration of sample properties, proving c-AFM and s-SNOM to be viable and destruction-free techniques for the identification of local 2DEG formation. Furthermore, applying c-AFM and s-SNOM in this manner opens the exciting prospect to link macroscopic low-temperature transport to its nanoscopic origin.

Received 12th March 2021
Accepted 2nd June 2021

DOI: 10.1039/d1na00190f

rsc.li/nanoscale-advances

Oxide interface electronics are an exciting possibility to implement highly correlated physics phenomena into modern electronics with the possibility to combine and access new functionality in electronic devices.[1,2] The $LaAlO_3/SrTiO_3$ (LAO/STO) system is one of the most investigated oxide heterostructures, as the two-dimensional electron gas (2DEG) at its interface holds astonishing properties, such as high mobility at low temperatures, gate-tunable conductivity, even the usually exclusive ferromagnetism and superconductivity. All of these properties are accessible in one confined electronic system.[3–6] The 2DEG forms by charge transfer, avoiding the polarity mismatch induced by LAO deposition on TiO_2-terminated STO. Residing on the STO side,[7] the resulting properties of the 2DEG are strongly dependent on the balance between ionic and electronic charge transfer, which both compensate the polarity mismatch.[8] This balance is determined by prior treatment of the STO substrate, subsequent thin film deposition parameters[5,7,9–14] and post-deposition treatment.[15–19] Another aspect is the stacking order of the atomic planes at the interface, which is determined by the termination of the STO substrate. In LAO/STO, the interfacial stacking order of TiO_2/LaO gives rise to a negative diverging potential, leading to electron transfer into the STO side of the interface (also called n-type). The predicted counterpart caused by a SrO/AlO_2 stacking order (p-type interface),[20] is still a debated topic. Even though recent results show a hole gas can be achieved,[21,22] p-type interfaces usually turn out to be insulating.[3,23–25] This behavior is commonly explained by a preferential ionic compensation of the potential by incorporation of oxygen vacancies.[26–28] As a result, even enhanced oxygen ion conductivity was proposed for this interface.[29] Vertically to these interfaces, the electronic to ionic charge transfer and carrier distribution has been investigated in great detail at present, however, in the lateral dimension it is less intensely studied.

To improve the understanding of the lateral 2DEG distribution, local probing of the interface properties becomes

[a]*Institute of Electronic Materials (IWE II), RWTH Aachen University, Aachen, Germany*
[b]*Peter Gruenberg Institute, JARA-FIT, Forschungszentrum Juelich GmbH, Juelich, Germany. E-mail: m.rose@fz-juelich.de; f.gunkel@fz-juelich.de*
[c]*I. Institute of Physics (IA), RWTH Aachen University, Aachen, Germany*

† Electronic supplementary information (ESI) available. See DOI: 10.1039/d1na00190f

a valuable tool. Until now, the 2DEG is typically understood as completely homogeneous on the lateral scale. Only at low temperatures, domain structures could be observed due to the STO phase transition to tetragonal crystal symmetry.[30–32] In this study, we are using conductive atomic force microscopy (c-AFM) complemented by scattering-type scanning near-field optical microscopy (s-SNOM), to test the assumption of lateral homogeneity at room temperature.

Recent results show that the STO surface terrace structure can induce anisotropic macroscopic transport in the 2DEG of Al_2O_3/STO.[33] A strong electrical transport anisotropy of the LAO/STO 2DEG could already be observed when the STO substrate surface holds an ordered, mixed termination.[34] Further works on the self-pattering of STO surfaces confirmed the mixed termination and highlight the ability to use this property to structure interfaces.[35,36] However, investigation of these naturally occurring inhomogeneities has not received much attention, even though research in this direction could potentially hold answers to open questions in the field: the above-mentioned lateral homogeneity of the 2DEG, causes of insulating interfacial areas, causes for sample-to-sample variation, and the role of an inhomogeneous 2DEG distribution for low-temperature phenomena. Utilizing a non-destructive technique, which allows subsequent investigation of samples by other methods to correlate macroscopic properties to local properties, opens the way to an enhanced understanding and functionality.

Scanning probe techniques are proven to extract detailed information across sample surfaces, exceeding the mere mapping of topography. It could be shown that phase differences in tapping AFM and lateral-force differences in contact AFM are able to distinguish chemical surface terminations.[36,37] Furthermore, s-SNOM has recently been shown to be able to optically detect free charge carriers in STO[38] as well as in LAO/STO heterostructures.[39–41] Both these established techniques (phase contrast AFM and s-SNOM) will be used to show how c-AFM can contribute to scientific advance in the field. Further scanning probe examples are scanning superconducting quantum interference device measurements, which revealed magnetic patches in LAO/STO that depend on the LAO thickness[42] and at low temperatures were able to identify highly conducting pathways,[31] and strain-tunable magnetic ordering.[32] Both phenomena correlate to the tetragonal STO domain walls forming below 105 K. Other techniques like Kelvin probe force microscopy showed the influence of oxygen vacancies on the band alignment of LAO/STO[14] as well as STO[43] and magnetic force microscopy showed the dependence of magnetic moments in LAO/STO on the electron density and thickness of the heterostructure.[44] Regarding c-AFM, it could be shown that conducting areas can be written into LAO/STO structures of subcritical thickness,[45–47] leading to the use of this effect as nano-patterning technique.[48] This in turn enabled researchers to easily fabricate one-dimensional systems to study exotic transport phenomena.[49] c-AFM was further used to determine the 2DEG confinement in cross-sectional measurements[7] and although it was also shown that c-AFM can be used to write conducting lines, it was not used to map naturally occurring differences of local conductivity distributions, and was not demonstrated with lateral resolution on the nanoscale.

We show in this study that c-AFM is a suitable technique to extract this local information of the LAO/STO 2DEG even though it is a buried structure. The lateral extraction of local information is on the scale of tens of nanometers and is obtained in a non-destructive manner, *i.e.* allowing the local mapping of conductivity without influencing interface properties. The high influence of the STO substrate surface

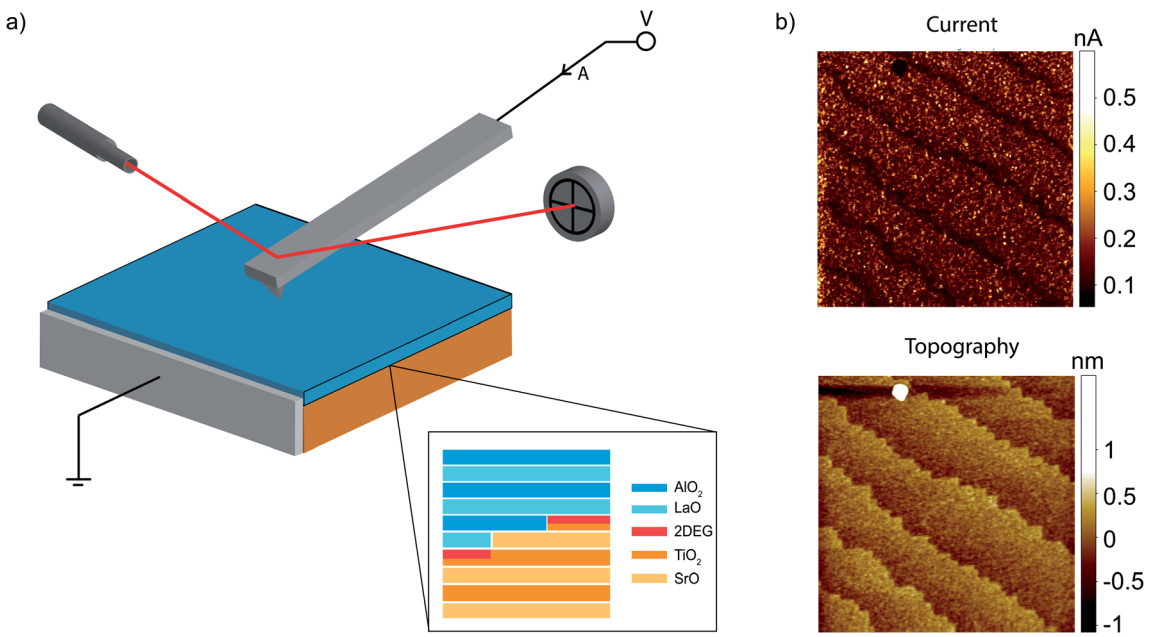

Fig. 1 (a) Shows a sketch of the c-AFM system with an inset depicting the atomic structure of the samples under test; (b) shows examples of measured topography and current maps for a LAO/STO sample. Both images are 1 × 1 μm in size.

termination on the interface conductivity is used to show how this local probing technique can directly correlate electronic transport properties to topographic features. In this way the interplay between STO topography and interfacial transport can be analyzed, leading to further insight into local 2DEG formation distribution in oxide heterostructures. Using s-SNOM, we furthermore corroborate that the lack of conductivity observed at SrO-terminated step terraces can be related to a diminished 2DEG density, rather than enhanced local thickness variation of the LAO overlayer. Therefore, the origin of macroscopic transport differences in identically fabricated heterostructures down to low-temperature conductivity can be linked to the nanoscopic origin of the 2DEG distribution.

A sketch of the c-AFM experimental setup is displayed in Fig. 1a. The working principle is that of classical AFM with an applied side electrode to access the laterally formed 2DEG. A voltage is applied between the doped diamond-coated AFM tip and bottom electrode while recording the current, making a parallel mapping of conductivity and topography possible. c-AFM measurements were performed in a cluster tool, where samples can be transferred *in situ* from the deposition chamber to the analytical methods. As samples are not exposed to air this way, the effects of adsorbates stemming from surface contaminations due to *e.g.* humidity can be excluded.[50–53]

An example of the current and topographic contrast of a LAO/STO sample is given in Fig. 1b. In order to probe local 2DEG formation, we specifically selected STO substrates which show distinct discrepancies from the characteristic TiO_2 topography as is shown in Fig. 1b.[54] To achieve this ordered, mixed termination, we make use of a bottom-up approach, exploiting the naturally occurring variance of single-crystalline STO. As-received STO single-crystalline substrates typically have a mixed surface termination after they have been cut, polished, and annealed. The fabrication of TiO_2-terminated STO *via* different routes has been intensively studied using chemical and heat treatments.[36,55–58] One common route is a wet etching treatment where water is applied to the surface, forming strontium hydroxide. A consecutive etching step in buffered hydrofluoric acid removes the hydroxide, leading to a fully TiO_2-terminated surface.[55] Consecutive annealing leads to the formation of an evenly distributed terrace-step structure when temperature, time and atmosphere are set correctly.[54,59–61] However, the properties of the as-received STO single crystals such as miscut angle[56,62–64] and defect concentration,[65] have high impact on the surface reconstruction, influencing the final result of combined chemical and thermal treatment. For this reason, the same treatment can commonly lead to different termination ratios, when applying the same process on different STO crystals.[36,66] The single-crystalline STO (100) substrates used here, were etched in buffered hydrofluoric acid for 2:30 minutes and subsequently annealed for 2 hours at 950 °C. Other routes, such as microwave-induced hydrothermal treatments are alternatives to this etching procedure to achieve a TiO_2 termination but require special equipment.[63,67]

The presence of two different STO surface terminations was identified using phase contrast in ambient AFM measurements. In Fig. 2a, the working principle of such a phase contrast under constant amplitude imaging is shown. As the tip-to-sample interaction force depends on surface chemistry, a local variation of termination induces an additional phase difference between driver and measured signal.[68] An example of this behavior is summarized in Fig. 2b–d. The topography image (Fig. 2b) shows rectangular topographic features present at the terrace edges in a 90° angle to each other. The surface roughness of the terrace planes is slightly higher than on the topographic features, which might influence the measured phase contrast. This is also reflected by slightly lower noise in the amplitude signal (Fig. 2c), which otherwise stays constant except for sharp lines when the tip reaches the edge of topographic height differences. Still, the phase image (Fig. 2d) shows a strong and sharply resolved contrast that extends from the edges of the terrace structure. While from one terrace plane to the next, height differences of roughly 0.4 nm are observed, the topographic features show clear plateaus of lower heights, showing that the observed phase contrast can be linked to the surface termination. Corresponding line profiles can be found in the ESI 1.† Here, we focus on the phase contrast, as it allows to visualize the termination distribution, which is helpful for later comparison to conductivity maps in c-AFM. A widening of the phase contrast along the lateral, topographic features is also visible by comparing cross-sectional line profiles of the three cases, which are provided in ESI 2.† Hence, the rectangular features can be identified as surfaces of different local chemistry than the rest of the sample surface.

Three distinct cases were observed, which will be referred to as case [A], [B], and [C] STO substrates (for STO) or LAO/STO samples (for LAO/STO) in the further discussion and are shown in Fig. 2e–g. An example of a case [A] STO substrate, which represents a complete TiO_2 termination, is shown in Fig. 2e. This case is discernable through evenly distributed, smooth terraces. A case [B] STO substrate is shown in Fig. 2f. These substrates turned out to have kinked terrace edges that differ from the ideal case [A] STO substrate. As was shown in Fig. 2d, these straight features indicate a termination change present at the terrace edges, relating to a SrO-termination in the case of STO.[69] Case [C] STO substrates show more pronounced features as is evident by the more extended regions in phase contrast shown in Fig. 2g. They reach out from the terrace edges and extend over the terrace planes, in some cases even across multiple terrace steps, having a higher coverage of SrO termination than case [B] STO substrates. From the surface topography, it can be judged that the three observed substrate cases hold different degrees of miscut angle and orientation. Note, that this property influences the surface physics beyond the observed SrO termination *e.g.* in respect to surface energy and therefore might also influence the observed interface phenomena. As the interfacial transport properties of LAO/STO heterostructures depend on substrate termination,[3] it can be expected that such SrO-terminated regions should be insulating. Therefore, *in situ* c-AFM is applied on LAO/STO samples of mixed substrate termination to open the possibility to map the 2DEG by monitoring the local conductivity.

On each of these substrates, 4 unit cells (uc) of LAO were deposited using pulsed laser deposition (PLD) (see

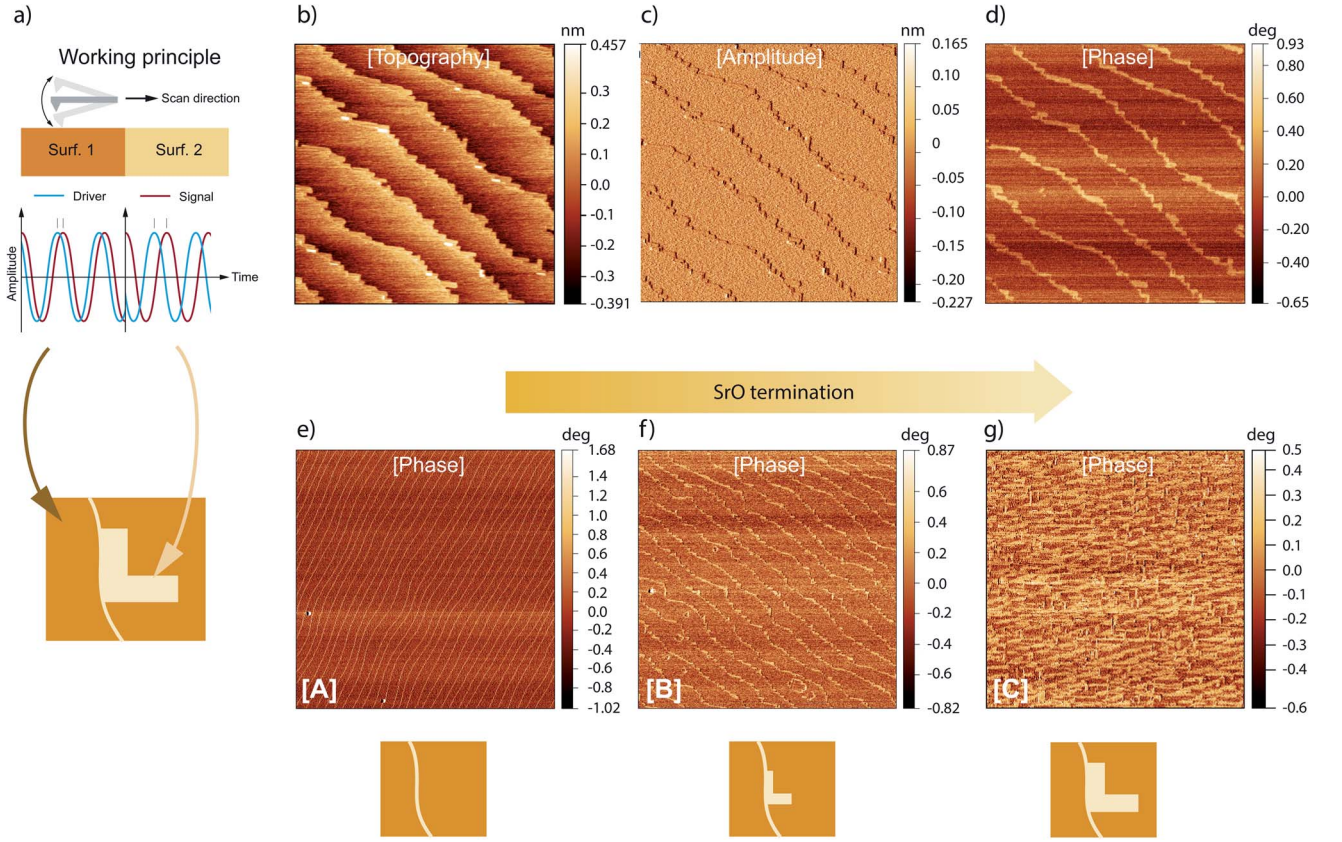

Fig. 2 STO substrates are shown with different termination distributions. All were etched with buffered HF acid and consecutively annealed at 950 °C for 2 h; (a) shows a sketch of the working principle of phase contrast in tapping AFM; (b) topography (c) amplitude and (d) phase of the same measurement are shown for a sample with two different surface terminations. These images (b–d) are 2 × 2 μm in size; phases are shown for samples with (e) full TiO_2 termination (case [A]), (f) partial secondary termination (case [B]), (g) mixed termination (case [C]). These images (e–g) are 5 × 5 μm in size.

Experimental section for details), monitored by high pressure reflective high-energy electron diffraction (RHEED). Distinct and clear RHEED intensity oscillations were observed throughout the entire thin film growth, indicating layer-by-layer growth mode for all samples. A detailed characterization of thin film growth can be found in ESI 3.† A LAO layer thickness of 4 uc

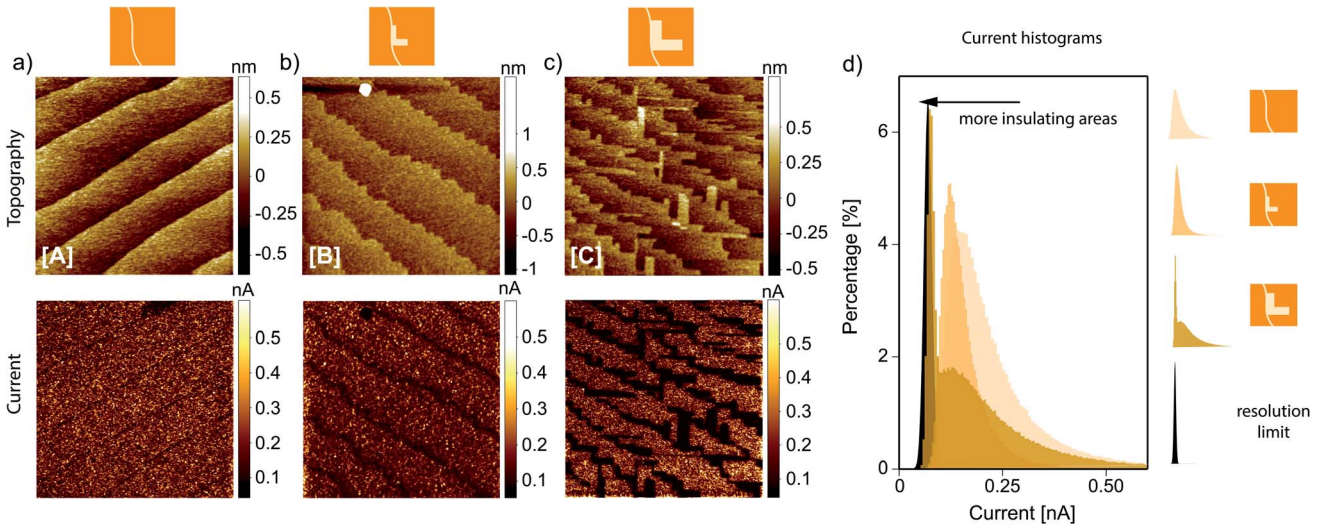

Fig. 3 Topography and current maps of samples consisting of 4 uc LAO on STO with different SrO to TiO_2 ratios measured by c-AFM; (a) full TiO_2 termination; (b) partial SrO termination (c) mixed termination. (d) Shows the current map histograms corresponding to the recorded images in (a)–(c). All images are 1 × 1 μm in size.

resembles the minimum thickness that leads to the formation of a 2DEG[4] and was chosen to minimize the required voltages for a detectable current through the LAO layer in subsequent c-AFM measurements. Test samples with subcritical LAO thickness of 3 uc were fabricated and electrically characterized to ensure the absence of underlying bulk conductivity. Furthermore, measurable current can only be detected if an electrical contact between 2DEG and bottom electrode is assured. This was achieved by applying a side contact, the removal of which again results in a lack of measurable current as shown in ESI 4.† This experiment proves that current is transferred through the 2DEG to the ground electrode, showcasing that interfacial conductivity is accessed using this setup.

The results of c-AFM analysis of 4 uc LAO deposited on case [A], [B] and [C] substrates can be found in Fig. 3a, b and c respectively. The topography of the deposited LAO thin films retains the same structural features present on the underlying substrates, as is expected for LAO thin films of this thickness. Therefore, it is assumed that the substrate topography is not changed by LAO growth. The applied voltage was set to 4 V as lower voltages lead to insufficient currents and higher voltages influence thin film morphology and sample properties.[43,70–72] The current maps show a distinct lateral contrast that is only visible for samples that were grown on case [B] and [C] STO substrates, where a partial SrO termination resides at the interface (Fig. 3b and c). For case [A] LAO/STO samples, a homogeneous current map was observed as shown in Fig. 3a. The detected contrast in case [B] and [C] LAO/STO samples directly correlates with structures that differ from the smooth terrace structure of case [A] LAO/STO samples. The kinked edges of case [B] LAO/STO samples appear as dark regions in the current maps and the same behavior is observable for the more pronounced features of case [C] LAO/STO samples. The transition from homogeneous currents to increasing insulating areas is also visible in cross-sectional line profiles, which are shown in ESI 5.† Note that the contrast is neither influenced by prolonged scan times nor by the scanning direction, indicating no sample alteration or measurement artefacts through the induced current. The qualitatively same result is achieved using samples with higher LAO thickness, showing that the observed phenomena are not caused by a local thickness variation (see ESI 6†). Significantly lower currents are achieved using thicker LAO layers, which is why they were not used to study the local 2DEG distribution. A tunneling mechanism is most likely responsible for current in these structures, as the recorded $I(V)$ curves show a symmetric current characteristic with the applied voltage (see ESI 7†) and behave similar to expected $I(V)$ curves in MOS structures.[73,74] In macroscopic tunnel junction measurements, direct tunneling was observed by Singh-Bhalla *et al.*[75] for the lower voltage regime, which transitioned into Fowler–Nordheim tunneling for the higher voltage regime when similar LAO thicknesses were used. Analyzing the $I(V)$ characteristic (see ESI 7†), revealed a similar behavior for low voltages, however, judging from the $I(V)$ slope at higher voltages, the most likely conduction mechanism is Poole–Frenkel emission (trap-assisted tunneling) for the used setup and samples. The role of trap-assisted tunneling was also determined by Swartz *et al.*[76] to have a high impact on the electrical transport through LAO thin films. This suggests that a convolution of direct tunneling and trap-assisted tunneling mechanisms is necessary to describe electrical transport in these experiments. In general, the $I(V)$ is comparable with literature and no degradation or alteration can be observed under these continuously applied voltages. Therefore, a breakdown is avoided if the voltage is not exceeding 4 V.

As current can only be achieved when the 2DEG is contacted (*via* metallic side electrode, *cf.* ESI 4†) and no bulk conductivity is present for these samples, the lack of current is caused by the absence of interfacial conductivity. Therefore, the c-AFM measurements shown in Fig. 3 confirm the nature of interfaces grown on the different substrate cases, as mixed conducting and insulating interfaces. The SrO-terminated regions of STO substrates, determined from phase contrast AFM, lead to a SrO/LaO stacking order, as can be seen by the rectangular features corresponding to the locally insulating parts of the samples.[77] Therefore, these results confirm to first degree the insulating behavior of SrO/AlO_2 interfaces and the possibility to have a resulting mixed conducting and insulating interface.

To give a more quantified evaluation of these current maps, the corresponding histograms are displayed in Fig. 3d, showing the distribution of measured currents. A reference sample without side electrode was added to visualize the resolution limit of the used setup (black area). The case [A] LAO/STO sample has the maximum of its current distribution set at the highest currents, which is expected because of the evenly distributed 2DEG. The case [B] LAO/STO sample shows similar behavior where the maximum is shifted to lower currents as one would expect for a sample with lower conductivity. The case [C] LAO/STO sample shows a strikingly different distribution of current. This results from the extended dark regions that are close to the measurement limit of our setup and are visible in the histogram as a peak around the noise level of $I \approx 100$ pA. Despite the overall low currents, none of them are below the resolution limit and thus extended dark regions are effectively insulating.

To further analyze if the source of electronically induced contrast is induced *via* a diminished carrier density, a sample that did show contrast in c-AFM was analyzed using s-SNOM. This scanning probe technique allows the determination of local optical properties with nanoscale resolution and high surface sensitivity.[78–80] The working principle is based on a laser beam focused on a metal-coated AFM tip (Fig. 4a), leading to strong near-fields which interact *via* dipole–dipole coupling with the sample. Backscattered light is demodulated at higher harmonics $n\Omega$ of the tapping frequency Ω and contains information about the dielectric function of the sample surface[81] while enabling tomographic probing depths of up to ~100 nm.[82–85] In the past, s-SNOM was shown to detect the presence of the 2DEG in LAO/STO[40] and even allow for determination of electronic properties (carrier density and mobility) using spectroscopy at different wavelengths.[39,41] Here, a correlative s-SNOM measurement on a 5 uc LAO/STO sample grown on a case [C] STO substrate is presented at a laser wavelength of $\lambda = 10.3$ μm ($\nu = 974$ cm^{-1}). As s-SNOM analysis is not hindered by the LAO thickness, 5 uc were chosen to avoid working at the critical thickness of LAO/STO. A distinct pattern of

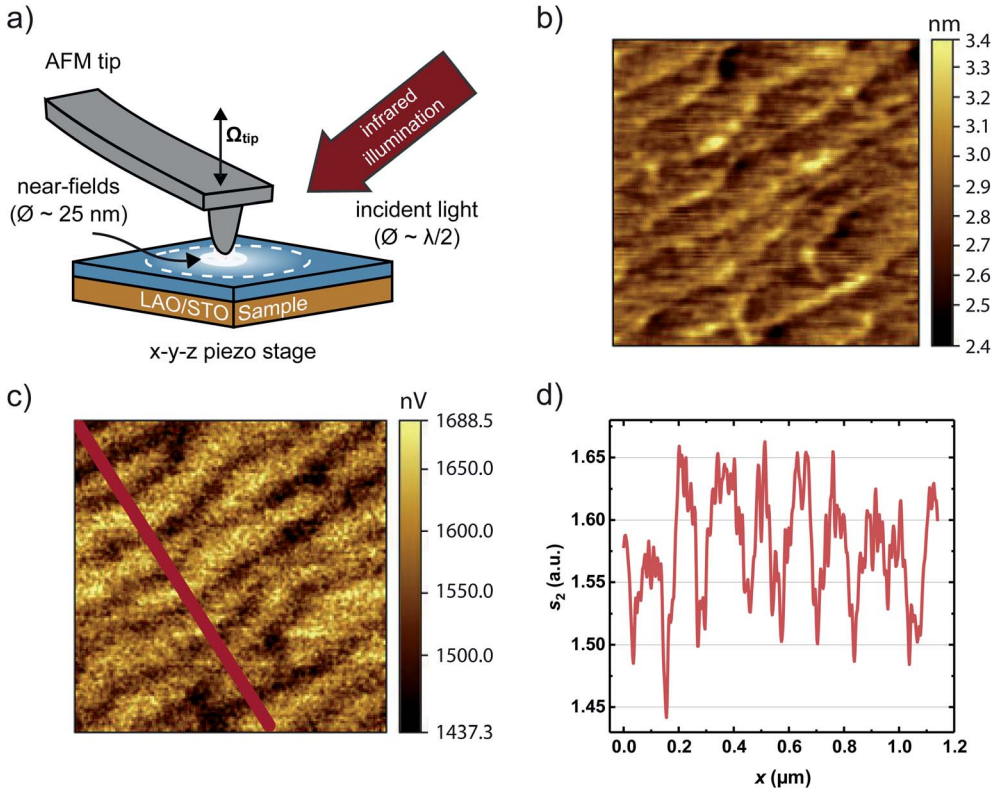

Fig. 4 (a) A sketch of the s-SNOM working principle is shown. (b) Shows the topography image of a 5 uc LAO/STO sample grown on a case [C] STO substrate with the corresponding optical image shown in (c). Both images are 1 × 1 μm in size. From the same measurements, a single line profile of the optical signal is shown for the second order demodulation in (d).

bright stripes and dark lines is visible in the s_2 signal (Fig. 4c), which is the second harmonic demodulation order (demodulation at $n\Omega$ with $n = 2$) of the scattering amplitude s_n. The lateral resolution in s-SNOM is broadened compared to c-AFM due to the larger AFM tip radii introduced by metal coating. Still, the atomic step terrace structure is resolved. Topographical artefacts can be excluded (see ESI 8†), as the small step height of ~0.4 nm is much smaller than the s-SNOM signal decay length of 40 nm (see Fig. S9†) and since no correlative behavior of the cantilever tapping phase or amplitude could be detected. The pattern in the optical amplitude (Fig. 4c) coincides with the atomic step edges visible in the topography (Fig. 4b) and similar to the conductivity maps of c-AFM measurements (Fig. 3c) it is significantly broader than the step edges. These features show a contrast of 7–13% for s_2 (line profile in Fig. 4d), which coincides well with previously reported contrast in this spectral range.[39,40]

Due to the non-linear tip-sample interaction, the relation of electronic properties to the s-SNOM signal is not trivial, making simulations necessary for data interpretation. They reveal that varying carrier density and mobility can induce the measured amplitude contrast of the optical signal (see ESI 9† for details of the simulation). Therefore, the dark lines in Fig. 4c are consistent with regions of a diminished 2DEG, corroborating the interpretation of c-AFM. The combined results from phase contrast AFM, c-AFM and s-SNOM congruently show the distinct influence of partial SrO-terminated STO surfaces, leading to a local 2DEG formation in LAO/STO.

To link the c-AFM and s-SNOM measurements to macroscopic transport, we measured the low-temperature resistance for all three cases. For this purpose, sample pieces were cut into

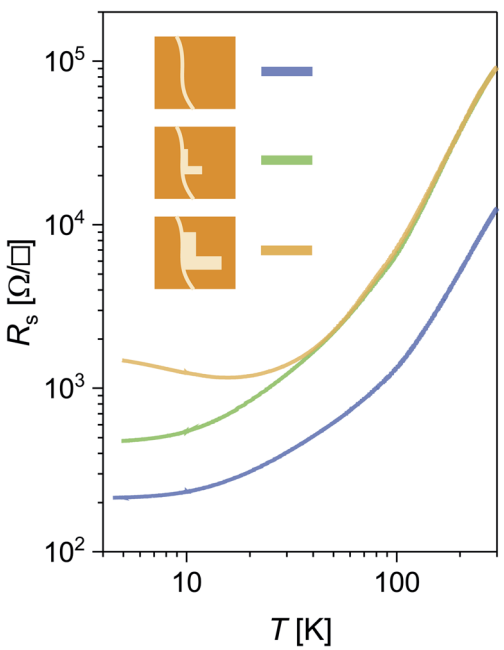

Fig. 5 Low-temperature resistivity measurements of a case [A], [B] and [C] LAO/STO sample.

a mimicked Hall bar geometry, where the terrace edges are aligned diagonal to the applied current. The results are summarized in Fig. 5. The resistance of the case [A] LAO/STO sample decreases with a decreasing temperature and reaches a constant value of about 200 Ω at 5 K, showing a metallic behavior. A similar behavior can be observed for the case [B] LAO/STO sample but shifted to overall higher resistances. In this case the metal-like behavior is observable with a residual resistance of about 400 Ω at 5 K. Again, the case [C] LAO/STO sample shows distinctly different behavior. At higher temperatures it overlaps with the data obtained for the case [B] LAO/STO sample, but with decreasing temperature it deviates in a resistance upturn and settles at about 2000 Ω at 5 K, showing a Kondo-like behavior.[5,86] As the conducting landscape is interrupted by the insulating areas, the resistance upturn at lower temperatures could be related to a freeze-out of percolation pathways as the temperature is decreased (note that the dielectric constant of STO is strongly temperature-dependent).[87] The changed 2DEG confinement at low temperatures in combination with its lateral distribution could induce such a behavior. However, an exact modelling is difficult due to the sensitivity of the dielectric constant on temperature[87] and local electric fields.[88]

Therefore, the macroscopic conductivity is influenced by the nanoscopic structures measurable in c-AFM, as the highest resistance at low temperature correlates to the largest amount of insulating areas detected by c-AFM. Furthermore, from low-temperature Hall measurements, it can be extracted that not only the average carrier density is lowered but also significantly the mobility of charge carriers (see ESI 10† for additional data). From this point, it can be concluded that additional scattering mechanisms are introduced, which are most likely linked to the increased number of insulating areas the electrons have to overcome, when passing through the sample. The correlation between insulating areas and resistance shows that the electrical conductivity from room- to low-temperature is significantly reduced by the introduction of local inhomogeneities. These inhomogeneities could only be identified through application of c-AFM, giving a simple method to identify relevant features that are only tens of nanometers large. Additionally, by using s-SNOM it can be confirmed that a lack of charge carriers at the topographic features could be a viable explanation for the measured contrast. The local inhomogeneities and their distribution throughout the 2DEG are directly influencing macroscopic transport behavior not only by lowering the conductance but giving rise to distinctly altered temperature behavior. Overall, the results are consistent with charge transfer being dependent on the local interface chemistry, leading to insulating behavior for SrO termination and metallic behavior only for TiO_2 termination of the used substrates.

Conclusion

We have demonstrated, for the example of the 2DEG model heterostructure LAO/STO, that *in situ* c-AFM can be used to not only access the buried 2DEG, but also to resolve lateral inhomogeneities on the nanometer scale. We have used this concept here to locally resolve atomic terrace phenomena at the LAO/STO interface. These terrace phenomena could be linked to a variation in termination that leads to a locally distributed 2DEG formation. The results show that one can access the buried two-dimensional conductivity with this technique, enabling a lateral resolution of features that are in the range of tens of nanometers but can be theoretically reduced to a few nanometers. Correlative s-SNOM measurements lead to the same conclusion, confirming the presented interpretation of the c-AFM results. In the future, s-SNOM spectroscopy of the 2DEG[41] could be used to quantify the local charge carrier density for inhomogeneities. In particular, simulations show that changes of the charge carrier density and mobility could yield a different spectroscopic response in this sample (*cf.* ESI 9†).

The presence of insulating as well as conducting areas on a nanoscale level result in significant alterations of the low-temperature behavior, emphasizing the impact of local inhomogeneities on low-temperature transport. The conductivity in these structures is not only decreased by the incorporation of insulating areas but altered into an upturn of resistance at the lowest temperatures for the more pronounced cases. Through the combined methods, the extended structural terrace features could be identified to act as scattering centers for electrons. This enables a destruction-free, nanoscopic and simple method to identify naturally occurring inhomogeneities on the lateral scale, which can be easily combined into the overall characterization of buried 2DEG systems. These results show how nanoscaled changes in a system have significant influence on the macroscopic scale and set a baseline for further studies towards the identification of causes for the natural inhomogeneities in local 2DEG formation.

Experimental

PLD process

All samples were grown in the same PLD chamber (Surface Systems and Technology GmbH & Co. KG, Germany) under the same nominal conditions. The substrates were bought from CrysTec GmbH Kristalltechnologie in Germany. Thin films were ablated from a single-crystalline LAO target that was placed at a distance of 54 mm from the STO substrates. The substrates were glued on sample holders using silver paste and heated up using an infrared laser heater system to 800 °C. For ablation, an excimer laser (248 nm) with a repetition rate of 1 Hz and a fluence of 0.96 J cm^{-2} was used. The deposition pressure inside the chamber was set to 1×10^{-3} mbar by inlet of oxygen gas, which was applied before heating. After growth, samples were left at deposition conditions for 1 hour to refill growth-induced oxygen vacancies and consecutively cooled down in deposition pressure.[7,10]

In situ c-AFM

Samples were transferred *in situ* into the c-AFM chamber using a cluster system. Here samples can be transferred to a pumped tunnel with a low base pressure of below 1×10^{-8} mbar. The

c-AFM is part of an Omicron VT-SPM system (Omicron Nano Technology GmbH) and was operated using a NANOSENSORS™ CDT-FMR tip ($C = 6.2$ N m^{-1}, $L = 225$ μm, $W = 27.5$ μm, $T = 3$ μm). The pressure inside the c-AFM system was always at 1×10^{-9} mbar during measurement. The tip was scanned with a speed of 1 μm s^{-1} under a force of 2 nN over the respective surfaces. For the shown measurements, a voltage of ±4 V was applied.

AFM

AFM measurements in ambient conditions were done using a Cypher AFM system from Asylum Research in tapping mode. The surfaces were scanned under a constant amplitude with a scanning speed of 5 μm s^{-1} at an image resolution of 512 × 512 pixels. The free amplitude in air was set to 109 nm, which was reduced to 87.2 nm in contact with the sample. Cantilevers provided by NanoAndMore (manufacturer NanoWorld) were used of the ARROW-NCR type ($f_0 = 285$ kHz, $C = 42$ N m^{-1}, $L = 160$ μm, $W = 45$ μm, $T = 4.6$ μm, $r < 10$ nm, Al coating on detector side).

s-SNOM

The s-SNOM measurement was done using a commercial microscope (neaSNOM, Neaspec GmbH) with a pseudoheterodyne module, a mercury cadmium telluride detector (InfraRed associates), and illumination at $\nu = 974$ cm^{-1} from a continuous wave CO_2 laser (Edinburgh Instruments) with a high signal-to-noise ratio. The topography signal and the near-field optical amplitude are recorded simultaneously and the optical amplitude s_n is demodulated at higher harmonics $n\Omega$ of the tip oscillation frequency $\Omega \approx 250$ kHz, with $n = 2$, to suppress background contributions. Commercially available AFM tips were used as scattering tips, in this case Pt–Ir-coated silicon tips with a tip radius of $r < 30$ nm (Arrow NCPt, NanoAndMore), and the tapping amplitude was adjusted to approximately $A = 35$ nm.

Low-temperature resistivity

The resistivity at low temperatures was measured using a PPMS system from Quantum Design. Sample contacts were achieved by wire bonding aluminum directly onto the sample surface. Samples were cooled down to 5 K while measuring the resistance in Hall bar geometry.

Conflicts of interest

There are no conflicts to declare.

References

1 J. Mannhart and D. Schlom, Oxide interfaces—an opportunity for electronics, *Science*, 2010, **327**, 1607–1611.
2 H. Y. Hwang, Y. Iwasa, M. Kawasaki, B. Keimer, N. Nagaosa and Y. Tokura, Emergent phenomena at oxide interfaces, *Nat. Mater.*, 2012, **11**, 103–113.
3 A. Ohtomo and H. Y. Hwang, A high-mobility electron gas at the $LaAlO_3/SrTiO_3$ heterointerface, *Nature*, 2004, **427**, 423–426.
4 S. Thiel, G. Hammerl, A. Schmehl, C. W. Schneider and J. Mannhart, Tunable quasi-two-dimensional electron gases in oxide heterostructures, *Science*, 2006, **313**, 1942–1945.
5 A. Brinkman, M. Huijben, M. Van Zalk, J. Huijben, U. Zeitler, J. C. Maan, W. G. Van der Wiel, G. Rijnders, D. H. A. Blank and H. Hilgenkamp, Magnetic effects at the interface between non-magnetic oxides, *Nat. Mater.*, 2007, **6**, 493–496.
6 N. Reyren, S. Thiel, A. D. Caviglia, L. F. Kourkoutis, G. Hammerl, C. Richter, C. W. Schneider, T. Kopp, A.-S. Ruetschi, D. Jaccard, M. Gabay, D. A. Muller, J.-M. Triscone and J. Mannhart, Superconducting interfaces between insulating oxides, *Science*, 2007, **317**, 1196–1199.
7 M. Basletic, J. Maurice, C. Carretero, G. Herranz, O. Copie, M. Bibes, E. Jacquet, K. Bouzehouane, S. Fusil and A. Barthelemy, Mapping the spatial distribution of charge carriers in $LaAlO_3/SrTiO_3$ heterostructures, *Nat. Mater.*, 2008, **7**, 621–625.
8 M.-A. Rose, B. Šmíd, M. Vorokhta, I. Slipukhina, M. Andrä, H. Bluhm, T. Duchon, M. Ležaic, S. A. Chambers, R. Dittmann, D. N. Mueller and F. Gunkel, Identifying Ionic and Electronic Charge Transfer at Oxide Heterointerfaces, *Adv. Mater.*, 2021, **33**, 2004132.
9 A. Kalabukhov, R. Gunnarsson, J. Borjesson, E. Olsson, T. Claeson and D. Winkler, Effect of oxygen vacancies in the $SrTiO_3$ substrate on the electrical properties of the $LaAlO_3/SrTiO_3$ interface, *Phys. Rev. B: Condens. Matter Mater. Phys.*, 2007, **75**, 121404.
10 C. Xu, C. Baeumer, R. A. Heinen, S. Hoffmann-Eifert, F. Gunkel and R. Dittmann, Disentanglement of growth dynamic and thermodynamic effects in $LaAlO_3/SrTiO_3$ heterostructures, *Sci. Rep.*, 2016, **6**, 22410.
11 C. Cancellieri, N. Reyren, S. Gariglio, A. D. Caviglia, A. Fete and J.-M. Triscone, Influence of the growth conditions on the $LaAlO_3/SrTiO_3$ interface electronic properties, *Europhys. Lett.*, 2010, **91**, 17004.
12 A. Fete, C. Cancellieri, D. Li, D. Stornaiuolo, A. D. Caviglia, S. Gariglio and J.-M. Triscone, Growth-induced electron mobility enhancement at the $LaAlO_3/SrTiO_3$ interface, *Appl. Phys. Lett.*, 2015, **106**, 51604.
13 F. Gunkel, C. Bell, H. Inoue, B. Kim, A. G. Swartz, T. A. Merz, Y. Hikita, S. Harashima, H. K. Sato, M. Minohara, S. Hoffmann-Eifert, R. Dittmann and H. Y. Hwang, Defect Control of Conventional and Anomalous Electron Transport at Complex Oxide Interfaces, *Phys. Rev. X*, 2016, **6**, 031035.
14 F. V. E. Hensling, D. J. Keeble, J. Zhu, S. Brose, C. Xu, F. Gunkel, S. Danylyuk, S. S. Nonnenmann, W. Egger and R. Dittmann, UV radiation enhanced oxygen vacancy formation caused by the PLD plasma plume, *Sci. Rep.*, 2018, **8**, 8846.
15 R. Moos and K. H. Härdtl, Defect chemistry of donor-doped and undoped strontium titanate ceramics between 1000 °C and 1400 °C, *J. Am. Ceram. Soc.*, 1997, **80**, 2549–2562.

16 T. Tanaka, K. Matsunaga, Y. Ikuhara and T. Yamamoto, First-principles study on structures and energetics of intrinsic vacancies in $SrTiO_3$, *Phys. Rev. B: Condens. Matter Mater. Phys.*, 2003, **68**, 205213.

17 R. Meyer, A. F. Zurhelle, R. A. De Souza, R. Waser and F. Gunkel, Dynamics of the metal-insulator transition of donor-doped $SrTiO_3$, *Phys. Rev. B*, 2016, **94**, 115408.

18 R. Merkle and J. Maier, How is oxygen incorporated into oxides? A comprehensive kinetic study of a simple solid-state reaction with $SrTiO_3$ as a model material, *Angew. Chem., Int. Ed.*, 2008, **47**, 3874–3894.

19 R. Waser and R. Hagenbeck, Grain boundaries in dielectric and mixed-conducting ceramics, *Acta Mater.*, 2000, **48**, 797–825.

20 R. Pentcheva and W. E. Pickett, Charge localization or itineracy at $LaAlO_3/SrTiO_3$ interfaces: hole polarons, oxygen vacancies, and mobile electrons, *Phys. Rev. B: Condens. Matter Mater. Phys.*, 2006, **74**, 35112.

21 H. Lee, N. Campbell, J. Lee, T. Asel, T. Paudel, H. Zhou, J. Lee, B. Noesges, J. Seo, B. Park, L. J. Brillson, S. H. Oh, E. Y. Tsymbal, M. S. Rzchowski and C.-B. Eom, Direct observation of a two-dimensional hole gas at oxide interfaces, *Nat. Mater.*, 2018, **17**, 231–236.

22 R. Pentcheva, M. Huijben, K. Otte, W. E. Pickett, J. E. Kleibeuker, J. Huijben, H. Boschker, D. Kockmann, W. Siemons, G. Koster, H. J. W. Zandvliet, G. Rijnders, D. H. A. Blank, H. Hilgenkamp and A. Brinkman, Parallel Electron-Hole Bilayer Conductivity from Electronic Interface Reconstruction, *Phys. Rev. Lett.*, 2010, **104**, 166804.

23 F. V. Hensling, C. Baeumer, M.-A. Rose, F. Gunkel and R. Dittmann, $SrTiO_3$ termination control: a method to tailor the oxygen exchange kinetics, *Mater. Res. Lett.*, 2020, **8**, 31–40.

24 H. Yan, J. M. Börgers, M.-A. Rose, C. Baeumer, B. Kim, L. Jin, R. Dittmann and F. Gunkel, Stoichiometry and Termination Control of $LaAlO_3/SrTiO_3$ Bilayer Interfaces, *Adv. Mater. Interfaces*, 2020, 2001477.

25 C. Baeumer, C. Xu, F. Gunkel, N. Raab, R. A. Heinen, A. Koehl and R. Dittmann, Surface Termination Conversion during $SrTiO_3$ Thin Film Growth Revealed by X-ray Photoelectron Spectroscopy, *Sci. Rep.*, 2015, **5**, 11829.

26 N. Nakagawa, H. Y. Hwang and D. A. Muller, Why some interfaces cannot be sharp, *Nat. Mater.*, 2006, **5**, 204–209.

27 J. N. Eckstein, Oxide interfaces - Watch out for the lack of oxygen, *Nat. Mater.*, 2007, **6**, 473–474.

28 F. Gunkel, R. Waser, A. H. H. Ramadan, R. A. De Souza, S. Hoffmann-Eifert and R. Dittmann, Space charges and defect concentration profiles at complex oxide interfaces, *Phys. Rev. B*, 2016, **93**, 245431.

29 F. Gunkel, D. V. Christensen and N. Pryds, Charge-transfer engineering strategies for tailored ionic conductivity at oxide interfaces, *J. Mater. Chem. C*, 2020, **8**, 11354.

30 M. Honig, J. A. Sulpizio, J. Drori, A. Joshua, E. Zeldov and S. Ilani, Local electrostatic imaging of striped domain order in $LaAlO_3/SrTiO_3$, *Nat. Mater.*, 2013, **12**, 1112.

31 B. Kalisky, E. M. Spanton, H. Noad, J. R. Kirtley, K. C. Nowack, C. Bell, H. K. Sato, M. Hosoda, Y. Xie, Y. Hikita, C. Woltmann, G. Pfanzelt, R. Jany, C. Richter, H. Y. Hwang, J. Mannhart and K. A. Moler, Locally enhanced conductivity due to tetragonal domain structure in $LaAlO_3/SrTiO_3$ heterointerfaces, *Nat. Mater.*, 2013, **12**, 1091.

32 D. V. Christensen, Y. Frenkel, Y. Z. Chen, Y. Xie, Z. Chen, Y. Hikita, A. Smith, L. Klein, H. Hwang, N. Pryds and B. Kalisky, Strain-tunable magnetism at oxide domain walls, *Nat. Phys.*, 2019, **15**, 269–274.

33 K. Wolff, R. Schäfer, D. Arnold, R. Schneider, M. Le Tacon and D. Fuchs, Influence of the vicinal substrate miscut on the anisotropic two-dimensional electronic transport in Al_2O_3-$SrTiO_3$ heterostructures, *J. Appl. Phys.*, 2020, **128**, 085302.

34 M. Foerster, R. Bachelet, V. Laukhin, J. Fontcuberta, G. Herranz and F. Sanchez, Laterally confined two-dimensional electron gases in self-patterned $LaAlO_3/SrTiO_3$ interfaces, *Appl. Phys. Lett.*, 2012, **100**, 231607.

35 L. Aballe, S. Matencio, M. Foerster, E. Barrena, F. Sanchez, J. Fontcuberta and C. Ocal, Instability and Surface Potential Modulation of Self-Patterned (001) $SrTiO_3$ Surfaces, *Chem. Mater.*, 2015, **27**, 6198–6204.

36 F. Sanchez, C. Ocal and J. Fontcuberta, Tailored surfaces of perovskite oxide substrates for conducted growth of thin films, *Chem. Soc. Rev.*, 2014, **43**, 2272–2285.

37 G. Koster, G. Rijnders, D. H. A. Blank and H. Rogalla, Surface morphology determined by (001) single-crystal $SrTiO_3$ termination, *Physica C*, 2000, **339**, 215–230.

38 M. Lewin, C. Baeumer, F. Gunkel, A. Schwedt, F. Gaussmann, J. Wueppen, P. Meuffels, B. Jungbluth, J. Mayer, R. Dittmann, R. Waser and T. Taubner, Nanospectroscopy of Infrared Phonon Resonance Enables Local Quantification of Electronic Properties in Doped $SrTiO_3$ ceramics, *Adv. Funct. Mater.*, 2018, **28**, 1802834.

39 W. Luo, M. Boselli, J. Poumirol, I. Ardizzone, J. Teyssier, D. van der Marel, S. Gariglio, J.-M. Triscone and A. B. Kuzmenko, High sensitivity variable-temperature infrared nanoscopy of conducting oxide interfaces, *Nat. Commun.*, 2019, **10**, 2774.

40 L. Cheng, D. Wang, S. Dai, Y. Yan, X. Fan, L. Wei and C. Zeng, Near-field imaging of the $LaAlO_3/SrTiO_3$ interfacial conductivity, *J. Infrared Millim. Terahertz Waves*, 2017, **36**, 543–546.

41 J. Barnett, M.-A. Rose, G. Ulrich, M. Lewin, B. Kästner, A. Hoehl, R. Dittmann, F. Gunkel and T. Taubner, Phonon-Enhanced Near-Field Spectroscopy to Extract the Local Electronic Properties of Buried 2D Electron Systems in Oxide Heterostructures, *Adv. Funct. Mater.*, 2020, **30**, 2004767.

42 B. Kalisky, J. A. Bert, B. B. Klopfer, C. Bell, H. K. Sato, M. Hosoda, Y. Hikita, H. Y. Hwang and K. A. Moler, Critical thickness for ferromagnetism in $LaAlO_3/SrTiO_3$ heterostructures, *Nat. Commun.*, 2012, **3**, 922.

43 M. Andrä, F. Gunkel, C. Bäumer, C. Xu, R. Dittmann and R. Waser, The influence of the local oxygen vacancy concentration on the piezoresponse of strontium titanate thin films, *Nanoscale*, 2015, **7**, 14351–14357.

44 F. Bi, M. Huang, H. Lee, C.-B. Eom, P. Irvin and J. Levy, $LaAlO_3$ thickness window for electronically controlled magnetism at $LaAlO_3/SrTiO_3$ heterointerfaces, *Appl. Phys. Lett.*, 2015, **107**, 082402.

45 C. Cen, S. Thiel, G. Hammerl, C. W. Schneider, K. E. Andersen, C. S. Hellberg, J. Mannhart and J. Levy, Nanoscale control of an interfacial metal–insulator transition at room temperature, *Nat. Mater.*, 2008, **7**, 298–302.

46 Y. Xie, C. Bell, T. Yajima, Y. Hikita and H. Y. Hwang, Charge Writing at the $LaAlO_3/SrTiO_3$ Surface, *Nano Lett.*, 2010, **10**, 2588–2591.

47 M. Boselli, D. Li, W. Liu, A. Fête, S. Gariglio and J.-M. Triscone, Characterization of atomic force microscopy written conducting nanowires at $LaAlO_3/SrTiO_3$ interfaces, *Appl. Phys. Lett.*, 2016, **108**, 061604.

48 P. Irvin, J. P. Veazey, G. Cheng, S. Lu, C. Bark, S. Ryu, C.-B. Eom and J. Levy, Anomalous High Mobility in $LaAlO_3/SrTiO_3$ Nanowires, *Nano Lett.*, 2013, **13**, 364–368.

49 M. Briggeman, M. Tomczyk, B. Tian, H. Lee, J.-W. Lee, Y. He, A. Tylan-Tyler, M. Huang, C.-B. Eom, D. Pekker, R. S. K. Mong, P. Irvin and J. Levy, Pascal conductance series in ballistic one-dimensional $LaAlO_3/SrTiO_3$ channels, *Science*, 2020, **367**, 769–772.

50 S. Adhikari, A. C. Garcia-Castro, A. H. Romero, H. Lee, J.-W. Lee, S. Ryu, C.-B. Eom and C. Cen, Charge Transfer to $LaAlO_3/SrTiO_3$ Interfaces Controlled by Surface Water Adsorption and Proton Hopping, *Adv. Funct. Mater.*, 2016, **26**, 5453–5459.

51 Y. Xie, Y. Hikita, C. Bell and H. Y. Hwang, Control of electronic conduction at an oxide heterointerface using surface polar adsorbates, *Nat. Commun.*, 2011, **2**, 494.

52 F. Bi, D. F. Bogorin, C. Cen, C. W. Bark, J. Park, C.-B. Eom and J. Levy, "Water-cycle" mechanism for writing and erasing nanostructures at the $LaAlO_3/SrTiO_3$ interface, *Appl. Phys. Lett.*, 2010, **97**, 173110.

53 A. Staykov, S. Fukumori, K. Yoshizawa, K. Sato, T. Ishihara and J. Kilner, Interaction of SrO-terminated $SrTiO_3$ surface with oxygen, carbon dioxide, and water, *J. Mater. Chem. A*, 2018, **6**, 22662–22672.

54 G. Koster, B. L. Kropman, G. J. H. M. Rijnders, D. H. A. Blank and H. Rogalla, Quasi-ideal strontium titanate crystal surfaces through formation of strontium hydroxide, *Appl. Phys. Lett.*, 1998, **73**, 2920–2922.

55 M. Kawasaki, K. Takahashi, T. Maeda, R. Tsuchiya, M. Shinohara, O. Ishiyama, T. Yonezawa, M. Yoshimoto and H. Koinuma, Atomic Control of the $SrTiO_3$ Crystal Surface, *Science*, 1994, **266**, 1540–1542.

56 R. Bachelet, F. Sanchez, F. J. Palomares, C. Ocal and J. Fontcuberta, Atomically flat SrO-terminated $SrTiO_3$ (001) substrate, *Appl. Phys. Lett.*, 2009, **95**, 141915.

57 J. G. Connell, B. J. Isaac, G. B. Ekanayake, D. R. Strachan and S. S. A. Seo, Preparation of atomically flat $SrTiO_3$ surfaces using a deionized-water leaching and thermal annealing procedure, *Appl. Phys. Lett.*, 2012, **101**, 251607.

58 V. Leca, G. Rijnders, G. Koster, D. H. A. Blank and H. Rogalla, Wet Etching Methods for Perovskite Substrates, *MRS Online Proc. Libr.*, 2011, **587**, 36.

59 J. Nie, A. Shoji, M. Koyanagi, H. Takashima, N. Terada and K. Endo, Control of Step Arrays on Normal and Vicinal $SrTiO_3$(100) Substrates, *Jpn. J. Appl. Phys.*, 1998, **37**, L1014.

60 T. Ohnishi, K. Shibuya, M. Lippmaa, D. Kobayashi, H. Kumigashira, M. Oshima and H. Koinuma, Preparation of thermally stable TiO_2-terminated $SrTiO_3$(100) substrate surfaces, *Appl. Phys. Lett.*, 2004, **85**, 272–274.

61 G. Koster, B. L. Kropman, G. J. Rijnders, D. H. Blank and H. Rogalla, Influence of the surface treatment on the homoepitaxial growth of $SrTiO_3$, *Mater. Sci. Eng., B*, 1998, **56**, 209–212.

62 G. B. Cho, M. Yamamoto and Y. Endo, Investigation of Self-Organized Steps and Terraces in $SrTiO_3$(001) Substrate Inclined in [110] Direction by Scanning Tunneling Microscopy, *Jpn. J. Appl. Phys.*, 2004, **43**, 1555–1560.

63 R. Bachelet, F. Sanchez, J. Santiso, C. Munuera, C. Ocal and J. Fontcuberta, Self-Assembly of $SrTiO_3$(001) Chemical-Terminations: A Route for Oxide-Nanostructure Fabrication by Selective Growth, *Chem. Mater.*, 2009, **21**, 2494–2498.

64 G. B. Cho, Y. Kamada and M. Yamamoto, Studies of Self-Organized Steps and Terraces in inclined $SrTiO_3$ (001) Substrate by Atomic Force Microscopy, *Jpn. J. Appl. Phys.*, 2001, **40**, 4666.

65 M. Castell, Nanostructures on the $SrTiO_3$(001) surface studied by STM, *Surf. Sci.*, 2002, **516**, 33–42.

66 F. Gellé, R. Chirita, D. Mertz, M. V. Rastei, A. Dinia and S. Colis, Guideline to atomically flat TiO_2-terminated $SrTiO_3$(001) surfaces, *Surf. Sci.*, 2018, **677**, 39–45.

67 I. Velasco-Davalos, R. Thomas and A. Ruediger, Realization of single-termination $SrTiO_3$ (100) surfaces by a microwave-induced hydrothermal process, *Appl. Phys. Lett.*, 2013, **103**, 202905.

68 R. Garcia, Nanomechanical mapping of soft materials with the atomic force microscope: methods, theory and applications, *Chem. Soc. Rev.*, 2020, **49**, 5850–5884.

69 B. Voigtländer, *Scanning Probe Microscopy*, Springer-Verlag, Berlin, Heidelberg, 2015.

70 A. Kumar, T. M. Arruda, Y. Kim, I. N. Ivanov, S. Jesse, C. W. Bark, N. C. Bristowe, E. Artacho, P. B. Littlewood, C.-B. Eom and S. V. Kalinin, Probing Surface and Bulk Electrochemical Processes on the $LaAlO_3$-$SrTiO_3$ Interface, *ACS Nano*, 2012, **6**, 3841–3852.

71 T. Menke, R. Dittmann, P. Meuffels, K. Szot and R. Waser, Impact of the electroforming process on the device stability of epitaxial Fe-doped $SrTiO_3$ resistive switching cells, *J. Appl. Phys.*, 2009, **106**, 114507.

72 C. Baeumer, N. Raab, T. Menke, C. Schmitz, R. Rosezin, P. M. Müller, M. Andrä, V. Feyer, R. Bruchhaus, F. Gunkel, C. M. Schneider, R. Waser and R. Dittmann, Verification of redox-processes as switching and retention failure mechanisms in Nb:$SrTiO_3$/metal devices, *Nanoscale*, 2016, **8**, 13967–13975.

73 W. Frammelsberger, G. Benstetter, R. Stamp, J. Kiely and T. Schweinboeck, Simplified tunneling current calculation for MOS structures with ultra-thin oxides for conductive atomic force microscopy investigations, *Mater. Sci. Eng., B*, 2005, **116**, 168–174.

74 F.-C. Chiu, A Review on Conduction Mechanisms in Dielectric Films, *Adv. Mater. Sci. Eng.*, 2014, **2014**, 578168.

75 G. Singh-Bhalla, C. Bell, J. Ravichandran, W. Siemons, Y. Hikita, S. Salahuddin, A. F. Hebard, H. Y. Hwang and R. Ramesh, Built-in and induced polarization across $LaAlO_3/SrTiO_3$ heterojunctions, *Nat. Phys.*, 2011, **7**, 80–86.

76 A. G. Swartz, S. Harashima, Y. Xie, D. Lu, B. Kim, C. Bell, Y. Hikita and H. Y. Hwang, Spin-dependent transport across $Co/LaAlO_3/SrTiO_3$ heterojunctions, *Appl. Phys. Lett.*, 2014, **105**, 032406.

77 J. Nishimura, A. Ohtomo, A. Ohkubo, Y. Murakami and M. Kawasaki, Controlled Carrier Generation at a Polarity-Discontinued Perovskite Heterointerface, *Jpn. J. Appl. Phys.*, 2004, **43**, L1032.

78 T. Taubner, R. Hillenbrand and F. Keilmann, Performance of visible and mid-infrared scattering-type near-field optical microscopes, *J. Microsc.*, 2003, **210**, 311–314.

79 F. Keilmann and R. Hillenbrand, Near-field microscopy by elastic light scattering from a tip, *Philos. Trans. R. Soc. London, Ser. A*, 2004, **362**, 787–805.

80 A. Huber, N. Ocelic, T. Taubner and R. Hillenbrand, Nanoscale Resolved Infrared Probing of Crystal Structure and of Plasmon-Phonon Coupling, *Nano Lett.*, 2006, **6**, 774–778.

81 B. Knoll and F. Keilmann, Near-field probing of vibrational absorption for chemical microscopy, *Nature*, 1999, **399**, 134–137.

82 T. Taubner, F. Keilmann and R. Hillenbrand, Nanoscale-resolved subsurface imaging by scattering-type near-field optical microscopy, *Opt. Express*, 2005, **13**, 8893.

83 R. Jacob, S. Winnerl, H. Schneider, M. Helm, M. T. Wenzel, H.-G. von Ribbeck, L. M. Eng and S. C. Kehr, Quantitative determination of the charge carrier concentration of ion implanted silicon by IR-near-field spectroscopy, *Opt. Express*, 2010, **18**, 26206–26213.

84 K. Moon, H. Park, J. Kim, Y. Do, S. Lee, G. Lee, H. Kang and H. Han, Subsurface Nanoimaging by Broadband Terahertz Pulse Near-Field Microscopy, *Nano Lett.*, 2015, **15**, 549–552.

85 L. Mester, A. A. Govyadinov, S. Chen, M. Goikoetxea and R. Hillenbrand, Subsurface chemical nanoidentification by nano-FTIR spectroscopy, *Nat. Commun.*, 2020, **11**, 3359.

86 J. Ruhman, A. Joshua, S. Ilani and E. Altman, Competition between Kondo screening and magnetism at the $LaAlO_3/SrTiO_3$ interface, *Phys. Rev. B: Condens. Matter Mater. Phys.*, 2014, **90**, 125123.

87 H. Weaver, Dielectric properties of single crystals of $SrTiO_3$ at low temperatures, *J. Phys. Chem. Solids*, 1959, **11**, 274–277.

88 R. A. van der Berg, P. W. M. Blom, J. F. M. Cillessen and R. M. Wolf, Field dependent permittivity in metal-semiconducting $SrTiO_3$ Schottky diodes, *Appl. Phys. Lett.*, 1995, **66**, 697.